

# ENHANCING EFFICIENCY FOR UNSTEADY CFD COMPUTATIONS IN AERONAUTICS

Magnus Carlsson<sup>1</sup>, Peter Eliasson<sup>1</sup> & Per Weinerfelt<sup>1</sup>

<sup>1</sup>Saab, SE-581 88 Linköping, Sweden

#### **Abstract**

We present developments to increase the efficiency of CFD calculations with focus on unsteady calculations using Saab's in-house CFD solver M-Edge for unstructured grids. The approach is based on the implicit solution of a steady state problem in each time step where the numerical fluxes are linearized giving a large sparse Jacobian matrix which is inverted iteratively. We demonstrate that with a proper linearization of all components of the numerical fluxes combined with large time steps approaches quadratic rate of convergence. We also show that approximative linearization, under-relaxation and smaller time steps may degrade the convergence and efficiency substantially. We demonstrate the findings for unsteady flow cases of a pitching airfoil and vortex shedding from a cylinder.

Keywords: CFD, implicit time integration, convergence acceleration, unsteady computations

### 1. Introduction

Aerodynamic predictions at Saab are to a large extent carried out by large scale parallel computations by numerically solving the Navier-Stokes equations. An in-house tool, M-Edge, is used for the calculations that uses a finitte volume formulation of the governing equations on unstructured computtional grids [1]. Traditionally, explicit time marching towards steady state is used together with convergence acceleration techniques such as local timestepping, multigrid and line implicit time marching to make the iterative process efficient [2], [3]. Recently, a fully implicit approach for the time marching scheme has been developed in a colaboration between Saab and NSC [4]. This had lead to a substantial speed-up for steady state calculations for large-scale applications. The implicit approach is based on solving a preconditioned linear system approximately and iteratively using a Krylov subspace method. The implicit technique is employed for a steady state problem as well as for unsteady calculations in every global time step. A significant speed-up was obtained for these problems but may still be improved to further reduce the computing time.

Discretizing a nonlinear time dependent problem by means of a time accurate stable implicit method, leads to a large system of nonlinear algebraic equations that has to be solved in each global time step. This can be done by applying the implicit scheme used to solve a steady state problem. The scheme will approach a Newton method when the time step in the steady state solver is sufficiently large. Hence, a quadratic rate of convergence should be obtained provided that the initial solution is "close enough" to the final solution. This is the case for unsteady problems where the global time step is small. Furthermore, a very well converged solution will result in a more time accurate solution to the unsteady problem.

The paper is organized as follows: In the next section we present the finite volume scheme for unstructured grids, including the discretization of the inviscid and viscous fluxes. Then follows a section about steady state time integration. Then we outline the new implicit scheme using an exact representation of the flux Jacobian. Next, a section of how to extend the steady state solution technique to time accurate problems by dual time stepping follows. Furthermore, a Section describing the theory and how to estimate dynamic derivatives from time accurate simulations is presented. After that we present a short section on the M-Edge flow solver. Finally, we present a set of unsteady flow cases demonstrating the improved efficiency of the new scheme, followed by some concluding remarks.

## 2. Finite Volume Method

We consider the governing equations of the Navier-Stokes equations in integral form

$$\int_{V} \frac{\partial Q}{\partial t} dV + \oint_{\partial V} F dS = 0 \tag{1}$$

with the conservative variables Q (density, momentum and total energy) and F the sum of the convective and viscous terms of the underlying continuity, momentum and energy equations.

Consider the discrete counterpart of Equation (1) with a control volume  $V_i$  for an arbitrary discrete node with subscript i. The spatial discretization of the Navier-Stokes equations in Equation (1) using a finite volume formulation on an unstructured grid for this node may be written in semi-discrete form as follows:

$$V_{i}\frac{dQ_{i}}{dt} + \sum_{k \in i} F_{ik}S_{ik} + F_{i_{bc}}S_{i_{bc}} = V_{i}\frac{dQ_{i}}{dt} + R_{i}(Q) = 0$$
(2)

where  $Q_i$  contains the conservative variables for node i,  $F_{ik}S_{ik}$  is the flux between two connected nodes i and k (denoted  $k \in i$ ),  $F_{ibc}S_{ibc}$  is the boundary flux at node i. The boundary flux is only included if the node is located on a boundary in order to close the control volume. If node i is an interior node this term vannishes. The fluxes are summed up to the residual for node i,  $R_i(Q)$ . The formulation is a so-called dual grid formulation where a dual grid forms the control volume to a primary grid. As an example, Figure 1 illustrates the dual grid of a triangular grid. The dual grid is computed in a preprocessing step which results in a single control surface for each edge, e.g.  $S_{01}$  between nodes 0 and 1 in Figure 1. A more thorough description of the approach above can be found in e.g. [5]. In the following, we leave out sub index when we refer to an entire vector for all unknowns.

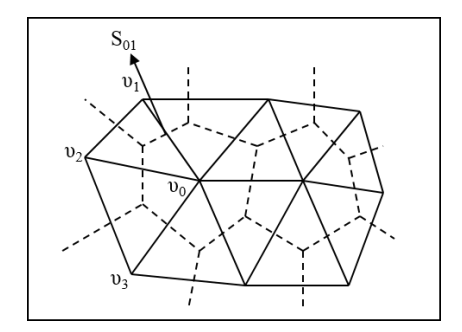


Figure 1 – Primary (solid line) triangular grid and its dual grid (dashed line).

# 2.1 Spatial Discretization

The schemes for the flux  $F_{ik}$  in Equation (2) considered here are based on a central discretization with dissipation terms for the inviscid part and a central discretization for the viscous part. The flux  $F_{ik}$  can then be formulated as

$$F_{ik} = F_{ik}^I + F_{ik}^V \tag{3}$$

## 2.1.1 Central Scheme with Artificial Dissipation

The inviscid flux across the cell face between nodes i and k is computed as

$$F_{ik}^{I} = F^{I}\left(\frac{Q_{i} + Q_{k}}{2}\right) - \frac{1}{2}d_{ik},$$
 (4)

where the function  $F^I$  is the physical central flux and  $d_{ik}$  denotes the artificial dissipation. A blend of second and fourth order differences are chosen as artificial dissipation with details according to Langer [6, 7]

$$d_{ik} = d_{ik}^{(2)} + d_{ik}^{(4)}. (5)$$

Here, the second order dissipation is formulated according to

$$d_{ik}^{(2)} = \lambda_{ik} \psi_{ik} (Q_i - Q_k) \tag{6}$$

where the local spectral raidus  $\lambda_{ik}$  is defined as

$$\lambda_{ik} = |u_{ik} \cdot n_{ik}| + c_{ik} \tag{7}$$

where  $u_{ik} = (u_i + u_k)/2$  and  $c_{ik} = (c_i + c_k)/2$  denote the cell face velocity and cell face speed of sound respectively. The normal direction of the control surface to the edge between nodes i and k is denoted by  $n_{ik}$ . The function  $\psi_{ik}$  is chosen to be active in the neighborhood of shocks and small in smooth regions of the flow

$$\psi_{ik} = \min \left[ \varepsilon^{(2)} \frac{(p_i - p_k)^2}{(p_i + p_k)^2}, 1 \right]. \tag{8}$$

In Equation (8), the sensitivity of the sensor is controlled by the parameter  $\varepsilon^{(2)}$  and  $p_i$  is the pressure. The fourth order dissipation is formulated as

$$d_{ik}^{(4)} = \lambda_{ik} \varepsilon^{(4)} (1 - \psi_{ik}) (\nabla^2 Q_i - \nabla^2 Q_k), \tag{9}$$

here  $\nabla^2$  denotes the undivided Laplacian operator and

$$\nabla^{2} Q_{i} = \sum_{k \in i} (Q_{i} - Q_{k}) = N_{i} Q_{i} - \sum_{k \in i} Q_{k}.$$
(10)

 $N_i$  is the number of neighbors of node i in Equation (10). Note that due to Equation (10), the discretization of Equation (9) involves all neighbors to node i and node k. The factor  $\varepsilon^{(4)}$  in Equation (9) is a global dissipation parameter and the factor  $(1 - \psi_{ik})$  ensures that the fourth order dissipation is switched off in the vicinity of shocks. In the following numerical tests, the tunable constants are chosen according to Langer,  $\varepsilon^{(2)} = 8$  and  $\varepsilon^{(4)} = 1/64$ .

# 2.1.2 Viscous Discretization

The viscous flux  $F^V$  is a function of the stress tensor  $\tau$ , the velocity u and the temperature gradient  $\nabla T$ . The stress tensor is formulated as

$$\tau = \mu \left[ \nabla u + (\nabla u)^T - \frac{2}{3}\mu(\nabla \cdot u)I \right]$$
(11)

where  $\mu$  is the dynamic viscosity,  $\nabla u$  the velocity gradient tensor,  $\nabla \cdot u$  the divergence of the velocity and I the unit matrix.

For the viscous flux between nodes i and k,  $F_{ik}^V = F_{ik}^V(\tau \cdot n_{ik}, u_{ik}, \nabla T \cdot n_{ik})$ , where  $n_{ik}$  is the unit normal vector for the control surface between the nodes. A thin-layer approach is used to approximate the part of the stress tensor containing normal derivatives [5], this can be expressed as

$$(\tau \cdot n_{ik})_{tl} = \mu \left[ \frac{\partial u}{\partial n_{ik}} + \frac{1}{3} \left( \frac{\partial u}{\partial n_{ik}} \cdot n_{ik} \right) n_{ik} \right]$$
 (12)

The normal derivative of an arbitrary quantity  $\phi$  between two nodes is approximated in a compact way as

$$\nabla \phi \cdot n_{ik} = \frac{\partial \phi}{\partial n_{ik}} \approx \frac{\phi_i - \phi_k}{|x_i - x_k|} \tag{13}$$

where  $|x_i - x_k|$  is the distance between the two nodes. This is applied to the normal velocity gradients in Equation (12) as well as to the normal derivative of the temperature in the energy equation. Remaining tangential derivatives of the stress tensor are obtained from nodal values of the velocity derivatives by the Gauss-Green relation approximated by the finite-volume formulation.

# 3. Implicit Time Integration

We are looking for a steady state solution in time to Equation (2). For steady fluid flow, time plays the role of an iteration parameter to achieve an asymptotic steady state solution in the computation. Therefore, the solution is advanced in time by an implicit backward Euler method.

The governing equations can then be expressed as:

$$(Q^{n+1} - Q^n)\frac{V}{\Lambda t} + R(Q^{n+1}) = 0.$$
(14)

Linearizing the residual leads to the following linear system of equations:

$$J(Q^n) \Delta Q^n = -R(Q^n) \tag{15}$$

with

$$J(Q^n) = \frac{V}{\Delta t}I + \frac{\partial R}{\partial Q}(Q^n), \quad \Delta Q^n = Q^{n+1} - Q^n.$$
 (16)

In practice, we employ an under-relaxation of the solution update:

$$Q^{n+1} = Q^n + \alpha \Delta Q^n, \quad \alpha \le 1 \tag{17}$$

To our findings,  $\alpha = 0.5$  offers a robust and efficient scheme. However, for time-accurate simulations it is desirable to employ no under-relaxation ( $\alpha = 1.0$ ) in order to speed up convergence.

The linear system of Equation (15) is solved by an iterative Krylov subspace method. In the present study, we employ the GMRES algorithm [8], preconditioned by an incomplete LU-factorization, namely ILU(0). For parallel processing, the ILU preconditioner is embedded in an additive Schwarz method. The implementation of the Krylov method is based on the PETSc software library [9] developed at Argonne National Laboratory.

# 3.1 Unsteady Time Integration

The steady state time integration schemes above can be extended to unsteady time accurate calculations by a so-called dual time stepping approach introducing a fictitious time derivative in dual time. We demonstrate this for the  $2^{nd}$  order backward difference scheme (BDF2) [10] that is employed in this paper. We stress that this approach can also be used other implicit schemes such as diagonally implicit multi-stage Runge-Kutta schemes [11] as well as fully implicit Runge-Kutta schemes [12]. The requirement is that the implicit scheme is both A- and L-stable.

We discretize Equation (2) with the BDF2 scheme, assuming that the geometry is fixed in time with a constant volume V,

$$V\frac{3Q^{n+1} - 4Q^n + Q^{n-1}}{2\Delta t} + R(Q^{n+1}) = 0.$$
(18)

We introduce a new time derivative in fictitious time  $\tau$  and denote the unknown  $Q^{n+1}$  with  $Q^*$ 

$$V\frac{dQ^*}{d\tau} + V\frac{3Q^* - 4Q^n + Q^{n-1}}{2\Delta t} + R(Q^*) = V\frac{dQ^*}{d\tau} + \tilde{R}(Q^*) = 0$$
(19)

where  $\tilde{R}(Q^*)=R(Q^*)+V(\frac{3}{2}Q^*-2Q^n+\frac{1}{2}Q^{n-1})/\Delta t$  and  $Q^*\to Q^{n+1}$  as  $\partial Q^*/\partial \tau\to 0$ . For each physical time step  $\Delta t$ , we can apply the steady state time integrator described above to Equation (19) to be iterated towards steady state in dual time  $\tau$ . It should be noted that for the implicit approaches described above, an additional contribution  $\frac{3V}{2\Delta t}I$  is added to the Jacobian.

The criterion for when the solution is sufficiently converged for each physical time step is based on the maximum norm of the density residual and is formulated as

$$||\tilde{R}(\rho^*)||_{\infty} < tol \tag{20}$$

where the iterations are interrupted when the maximum density residual (or dual time derivative of density) is below a given tolerance *tol* in the entire computational domain. For all unsteady CFD simulations carried out here, the convergence in dual time can be driven down toward the computer machine precision for all equations.

## 3.2 Jacobian Evaluation

The exact linearization of the spatial discretization can be complex. Amongst others, it requires the full linearization of the artificial dissipation operator (Equation (5)) which can be quite complicated to derive. Furthermore, the exact discretization of the fourth order operator in Equation (9) requires a wider stencil compared to a compact nearest neighbor stencil, thus increasing the memory requirement extensively. The expanded stencil will also increase data transfer across partitions in parallell simulation, since more neighbors have to be provided at partition edges. However, this is done in order to enhance the convergence for parallel computations as an exact representation of the Jacobian can provide an extreme decay of the residual and a converged solution within few iterations.

The linearization of the inviscid fluxes, the normal derivatives of the viscous fluxes, and the boundary fluxes are done exactly, i.e. no approximation is made. For the linearization of the artificial dissipation of the convective flux term, the dissipation operator is described in the following. Taking the partial derivative of the dissipation operator in Equation (5) with respect to  $Q_i$  gives

$$\frac{\partial d_{ik}}{\partial Q_i} = \frac{\partial d_{ik}^{(2)}}{\partial Q_i} + \frac{\partial d_{ik}^{(4)}}{\partial Q_i}.$$
 (21)

Here, j is a node that is part of the discretization of the dissipative flux between nodes i and k, e.g.  $j \in i, k, neigh_i, neigh_k$  where  $neigh_i, neigh_k$  are neighbor nodes to nodes i and k. An expanded form of the second order part (Equation (6)) can be written as

$$\frac{\partial d_{ik}^{(2)}}{\partial Q_i} = \frac{\partial \lambda_{ik}}{\partial Q_i} \psi_{ik} (Q_i - Q_k) + \lambda_{ik} \frac{\partial \psi_{ik}}{\partial Q_i} (Q_i - Q_k) + \lambda_{ik} \psi_{ik} \frac{\partial (Q_i - Q_k)}{\partial Q_i}$$
(22)

All terms on the right hand side of Equation (22) are non-zero if  $j \in i, k$  and the resulting stencil of the Jacobian due to the second order dissipation is compact. The derivatives  $\frac{\partial \lambda_{ik}}{\partial Q_j}$ ,  $\frac{\partial \psi_{ik}}{\partial Q_j}$  in Equation (22) can be evaluated by straight forward differentiation. A convenient way is to compute the derivative with respect to primitive variables  $(W_j)$  and then multiply with the transformation matrix from primitive variables to conservative variables:

$$\frac{\partial \lambda_{ik}}{\partial Q_i} = \frac{\partial \lambda_{ik}}{\partial W_i} \frac{\partial W_j}{\partial Q_i}, \quad \frac{\partial \psi_{ik}}{\partial Q_i} = \frac{\partial \psi_{ik}}{\partial W_i} \frac{\partial W_j}{\partial Q_i}.$$
 (23)

The derivative of the fourth order dissipation term (Equation (9)) can be written as

$$\frac{\partial d_{ik}^{(4)}}{\partial Q_j} = \frac{\partial \lambda_{ik}}{\partial Q_j} (1 - \psi_{ik}) (\nabla^2 Q_i - \nabla^2 Q_k) - \lambda_{ik} \frac{\partial \psi_{ik}}{\partial Q_j} (\nabla^2 Q_i - \nabla^2 Q_k) + \lambda_{ik} (1 - \psi_{ik}) \frac{\partial (\nabla^2 Q_i - \nabla^2 Q_k)}{\partial Q_j}$$
(24)

The two first terms on the right hand side of Equation (24) are non-zero if  $j \in i,k$ . The last term is non-zero for all neighbors of nodes i and k and needs further attention. By evaluating the derivative of the undivided laplacian (Equation (10)), we get

$$\frac{\partial(\nabla^2 Q_i - \nabla^2 Q_k)}{\partial Q_j} = \begin{cases} N_i + 1 & \text{if } j \in i \\ -(N_k + 1) & \text{if } j \in k \\ \pm 1 & \text{else} \end{cases}$$
 (25)

Here,  $N_i$  and  $N_k$  are the number of neighbors of node i and k, respectively, and we have used the right hand side of Equation (10) to evaluate the derivatives. As can be seen from Equation (25), a wider stencil including neighbor to neighbors will be present in the Jacobian matrix.

The full linearization of the dissipative flux will be compared to a simpler approximation of the Jacobian, assuming only second order dissipation, no dependence on the shock sensor and constant local spectral radius. The resulting Jacobian with respect to artificial dissipation can then be written as

$$\frac{\partial d_{ik}}{\partial Q_j} \approx \varepsilon^{(2)} \lambda_{ik} \frac{\partial (Q_i - Q_k)}{\partial Q_j} = \begin{cases} \varepsilon^{(2)} \lambda_{ik} & \text{if } j \in i \\ -\varepsilon^{(2)} \lambda_{ik} & \text{if } j \in k \end{cases}$$
(26)

Equation (26) is the derivative of Equation (6) using a constant  $\varepsilon^{(2)}$  instead of the shock sensor  $\psi_{ik}$  and no contribution from the fourth order dissipation. Using  $\varepsilon^{(2)} = 1$  corresponds to a first order upwind scheme.

# 4. Dynamic Derivatives

Flight mechanical simulation models require dynamic derivatives such as  $C_{N,\dot{\alpha}}=\frac{\partial C_N}{\partial \dot{\alpha}}$  where  $C_N$  is the normal force coefficient,  $\alpha$  is the angle of attack and  $\dot{\alpha}$  its velocity. Dynamic derivatives can be obtained from unsteady flow computations, the theory and computations of these are presented in this section.

# 4.1 Theory

The general description of a time dependent flow in Equation (2) can be extended to

$$\frac{dQ}{dt} + R(Q, \alpha, \dot{\alpha}) = 0 \tag{27}$$

where

$$\alpha(t) = \alpha_0 + \Delta \alpha(t), \quad \Delta \alpha(t) = \alpha_{amp} \sin(\omega t), \quad \Delta \dot{\alpha} = \alpha_{amp} \omega \cos(\omega t)$$
 (28)

and  $\alpha_0$  is the reference angle of attack,  $\alpha_{amp}$  is the amplitude of the pitching movement and  $\omega=2\pi f$  is the pitching frequency. The conservative variable Q is split in a steady and a time dependent part,  $Q(t)=\bar{Q}+\Delta Q(t)$ ,

$$R(Q,\alpha,\dot{\alpha}) \approx R(\bar{Q},\alpha_0,0) + \frac{\partial R}{\partial Q} \Delta Q + \frac{\partial R}{\partial \alpha} \Delta \alpha + \frac{\partial R}{\partial \dot{\alpha}} \Delta \dot{\alpha} = \frac{\partial R}{\partial Q} \Delta Q + \frac{\partial R}{\partial \alpha} \Delta \alpha + \frac{\partial R}{\partial \dot{\alpha}} \Delta \dot{\alpha}$$
 (29)

where the last equality follows from the fact that  $R(\bar{Q}, \alpha_0, 0) = 0$ . All derivatives in Equation (29) are evaluated at  $(\bar{Q}, \alpha_0, 0)$ . From Equations (27) and (29) we obtain the linear equation

$$\frac{d\Delta Q}{dt} + \frac{\partial R}{\partial Q}\Delta Q = -\frac{\partial R}{\partial \alpha}\Delta \alpha - \frac{\partial R}{\partial \dot{\alpha}}\Delta \dot{\alpha}$$
(30)

 $\Delta \alpha$  in Equation (28) together with the ansatz

$$\Delta Q(t) = Q^{c} \cos(\omega t) + Q^{s} \sin(\omega t) = \widehat{Q}^{c} \Delta \dot{\alpha} + \widehat{Q}^{s} \Delta \alpha$$
(31)

are inserted into Equation (30) which gives

$$-\omega^2 \widehat{Q}^c \Delta \alpha + \widehat{Q}^s \Delta \dot{\alpha} + \frac{\partial R}{\partial Q} \left( \widehat{Q}^c \Delta \dot{\alpha} + \widehat{Q}^s \Delta \alpha \right) = -\frac{\partial R}{\partial \alpha} \Delta \alpha - \frac{\partial R}{\partial \dot{\alpha}} \Delta \dot{\alpha}$$
(32)

Identifying  $\Delta\alpha$  and  $\Delta\dot{\alpha}$  terms on the left and right side in Equation (32) we obtain

$$\left(I\omega^{2} + \frac{\partial R}{\partial Q}\frac{\partial R}{\partial Q}\right)\widehat{Q}^{c} = -\frac{\partial R}{\partial Q}\frac{\partial R}{\partial \dot{\alpha}} + \frac{\partial R}{\partial \alpha}$$

$$\left(I\omega^{2} + \frac{\partial R}{\partial Q}\frac{\partial R}{\partial Q}\right)\widehat{Q}^{s} = -\frac{\partial R}{\partial Q}\frac{\partial R}{\partial \alpha} - \omega^{2}\frac{\partial R}{\partial \dot{\alpha}}$$
(33)

The time dependent pressure coefficient  $C_p$  and the force and moment coefficients  $C_X$  can be expressed in terms of  $\hat{Q}^c$  and  $\hat{Q}^s$  according to

$$C_{p}(Q) = C_{p}\left(\overline{Q} + \Delta Q\right) \approx C_{p}\left(\overline{Q}\right) + \frac{dC_{p}}{dQ}\Delta Q = C_{p}\left(\overline{Q}\right) + \frac{dC_{p}}{dQ}\widehat{Q}^{s}\Delta\alpha + \frac{dC_{p}}{dQ}\widehat{Q}^{c}\Delta\dot{\alpha} \Rightarrow$$

$$C_{X} = C_{X}\left(\alpha_{0}\right) + C_{X,\alpha}\Delta\alpha + C_{X,\dot{\alpha}}\Delta\dot{\alpha} \tag{34}$$

From Equation (33) we observe that  $\widehat{Q}^c$  and  $\widehat{Q}^s$  are functions of  $\omega^2$  which means that  $C_{X,\alpha}$  and  $C_{X,\dot{\alpha}}$  are also depending  $\omega^2$ . This implies that we can apply Richardson extrapolation to compute an accurate estimation of  $C_{X,\dot{\alpha}}$  when  $\omega^{\to}0$  with an asymptotic expansion of  $C_{X,\dot{\alpha}}$  in terms of  $\omega$  as

$$C_{X,\dot{\alpha}}(\omega) = C_{X,\dot{\alpha}}(0) + \sum_{k=1}^{N} C_{X,\dot{\alpha}}(2k)\omega^{2k}$$
 (35)

where  $C_{X,\dot{\alpha}}(2k), k = 0, 1, ..., N$  are unknown coefficients.

# 4.2 Estimations from Unsteady Computations

The dynamic derivatives in the previous section can be computed by employing a pitching movement in a rotating coordinate frame of reference by computing a local grid velocity according to

$$\vec{v}_{grid}(\vec{r},t) = \vec{\Omega}(t) \times (\vec{r} - \vec{r}_0). \tag{36}$$

Here,  $\Omega(t) = \vec{n}\Delta\dot{\alpha}(t)$  is the angular velocity,  $\Delta\dot{\alpha}(t)$  is given in Equation (28),  $\vec{n}$  is the axis of rotation,  $\vec{r}$  is the local grid coordinate and  $\vec{r}_0$  is the reference coordinate point for the rotation. The response in  $C_X$  given by the prescribed motion is computed by the ansatz in Equation (34). The ansatz assumes that given a small enough amplitude  $\alpha_{amp}$  in Equation (28) will yield a linear response in  $C_X$  with respect to the frequency  $\omega$ . The derivatives are computed from the time series of  $C_X$  by fitting a Fourier Series expansion of the  $C_X$  coefficient according to

$$\tilde{C}_X = A_0 + \sum_{n=1}^{N} \left( A_n \cos(n\omega t) + B_n \sin(n\omega t) \right). \tag{37}$$

A least-squares fit is used to compute the coefficient in Equation (37) with N=4. The terms containing the multiples of frequencies (n>1) are included in order to verify that they are indeed sufficiently close to zero.

# 5. The Flow Solver M-Edge

The CFD code employed for the present simulations and used internally at Saab is the M-Edge flow solver, which originates from the Edge flow solver [13]. The discretization in space is a finite volume formulation for unstructured grids as described above where a median dual grid forms the control volumes with the unknowns allocated in the grid nodes. Throughout this paper, a central discretization is used for both the convection and the viscous terms as described in Section 2.1 There are numerous boundary conditions available in M-Edge for walls, external boundaries and periodic boundaries. All of these boundary conditions are specified weakly, which means, that the unknowns on nodes located on a boundary are unknowns like any other unknown in the interior [2], [14]. The boundary conditions are specified through the boundary flux in Equation (2).

A preprocessor creates the dual grid, wall distances and other quantities required by the flow solver. Last but not least, it splits the computational grid by domain decomposition for parallell computations.

## 6. Numerical Results

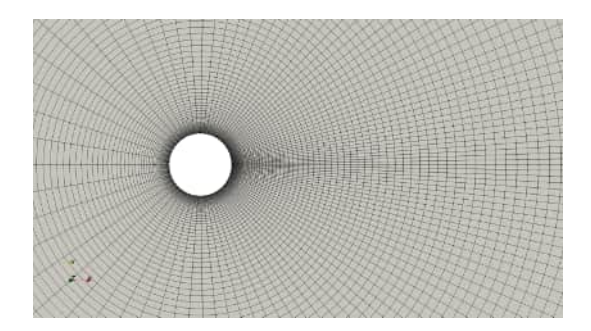
Numerical results are presented for laminar flow over a cylinder and Euler flow over a RAE2822 airfoil. All simulations are unsteady calculations using dual time stepping with the BDF2 method. The calculations of the cylinder case employ no-slip adiabatic wall conditions and slip wall for the airfoil case, and characteristic far field boundary conditions.

All numerical results are obtained using the central scheme with artificial dissipation as outlined in Section 2.1 the tunable constants are chosen to  $\varepsilon^{(2)}=8$  and  $\varepsilon^{(4)}=1/64$ . It is noted that the same values of the coefficients are used in the full linearization of the artificial dissipation. Comparisons are made between the computations obtained with the implicit scheme employing the exact linearization of the flux Jacobian using a wider stencil, and with an approximative Jacobian using a compact stencil. The numerical constant for the approximative Jacobian scheme is set to  $\varepsilon^{(2)}=1$ , which corresponds to a first order upwind scheme.

Unsteady calculations are given an initial flow solution and use  $CFL=10^6$  when computing the local time step. The under-relaxation factor is set to one, i.e. no under relaxation is used unless otherwise stated. The convergence of the density residual is displayed for both cases, the density residual is defined such that it corresponds to the dual time derivative of the density. The logarithm of the  $L_{\infty}$ -norm of the residual is displayed.

## 6.1 Unsteady Laminar Flow over a Cylinder

The first test case involves laminar flow over a cylinder at Re = 185 and  $M_{\infty} = 0.2$ . Three successively refined hexahedral grids of  $13 \times 10^3$ ,  $50 \times 10^3$  and  $160 \times 10^3$  are employed. The outer boundary is



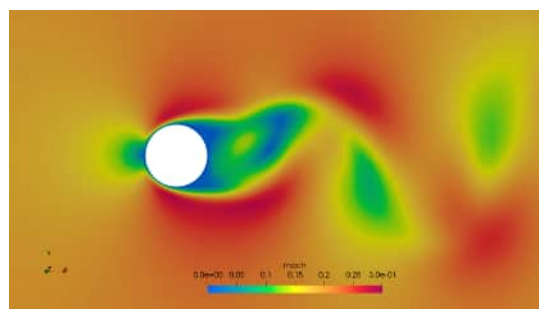


Figure 2 – Laminar flow over a cylinder at M = 0.2, Re = 185. Coarsest grid (left), Mach number contours (right).

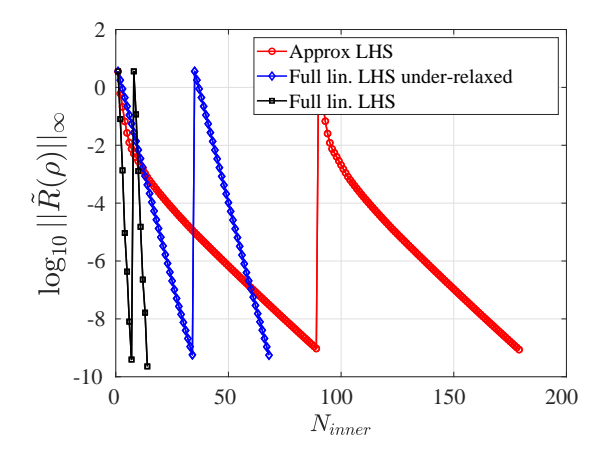


Figure 3 – Laminar flow over a cylinder at M=0.2, Re=185. Convergence of the density residual as a function of inner iterations. Two typical global time steps shown for  $\Delta t = T/20$ .

located far away from the cylinder at a distance of 250 diameters to reduce its influence on the flow and the integrated forces. The coarsest grid and the instantanaeous flow field are shown in Figure 2. The flow develops a periodic solution in time with vortex shedding. The Strouhal number approaches  $St = fD/U_{\infty} \approx 0.18$  with a sufficient temporal resolution where D is the cylinder diameter,  $U_{\infty}$  is the free stream velocity and f is the shedding frequency. The time dependent solutions are initialized from an initial solution where the periodic unsteadiness has developed and progress periodically for 10 periods using the smallest time step considered and a very strict convergence criterion (9 orders of residual decay in dual time). A comparison of the dual time convergence for two typical time steps of the approximative Jacobian, the exact Jacobian using under-relaxation ( $\alpha = 0.5$  in Equation (17)), and the exact Jacobian using no under-relaxation ( $\alpha = 1$ ) is shown in Figure 3. Altough each nonlinear iteration requires more linear iterations, the convergence rate is vastly different. For this case, the exact Jacobian scheme converges within 7 iterations per time step, whereas the under-relaxed exact Jacobian scheme requires 34 iteration and the approximative Jacobian scheme requires 90 iterations for the same convergence criterion.

Different convergence criteria are then applied to the initial solution and integrated in time for 2 periods. Various sizes of the time steps  $\Delta t = T/n$  are used where n = [20, 40, 80, 160, 320, 640] corresponding to the number of time steps  $\Delta t$  per period T. The solutions are compared to an "exact" solution using n = 640, starting from the same initial solution, integrated with the strictest convergence criterion (9 orders residual decay) in each stage. The investigation focuses on comparisons with integrated drag. Time evolution of drag for the different residual criteria can be seen in Figure 4. Improvement from the refinement of the time steps as well as the convergence criterion can be clearly seen. There is a good agreement with the reference solution at time steps  $\Delta t \leq T/80$ .

To quantify the level of convergence the error of the integrated drag is used. The error of the drag is computed as the L2-norm of the difference between the current and reference solution at each time step over the 1.5 periods of computing. Since a convergence criterion of the density residual is set, the average number of inner iterations are computed. The error of the integrated drag as a function

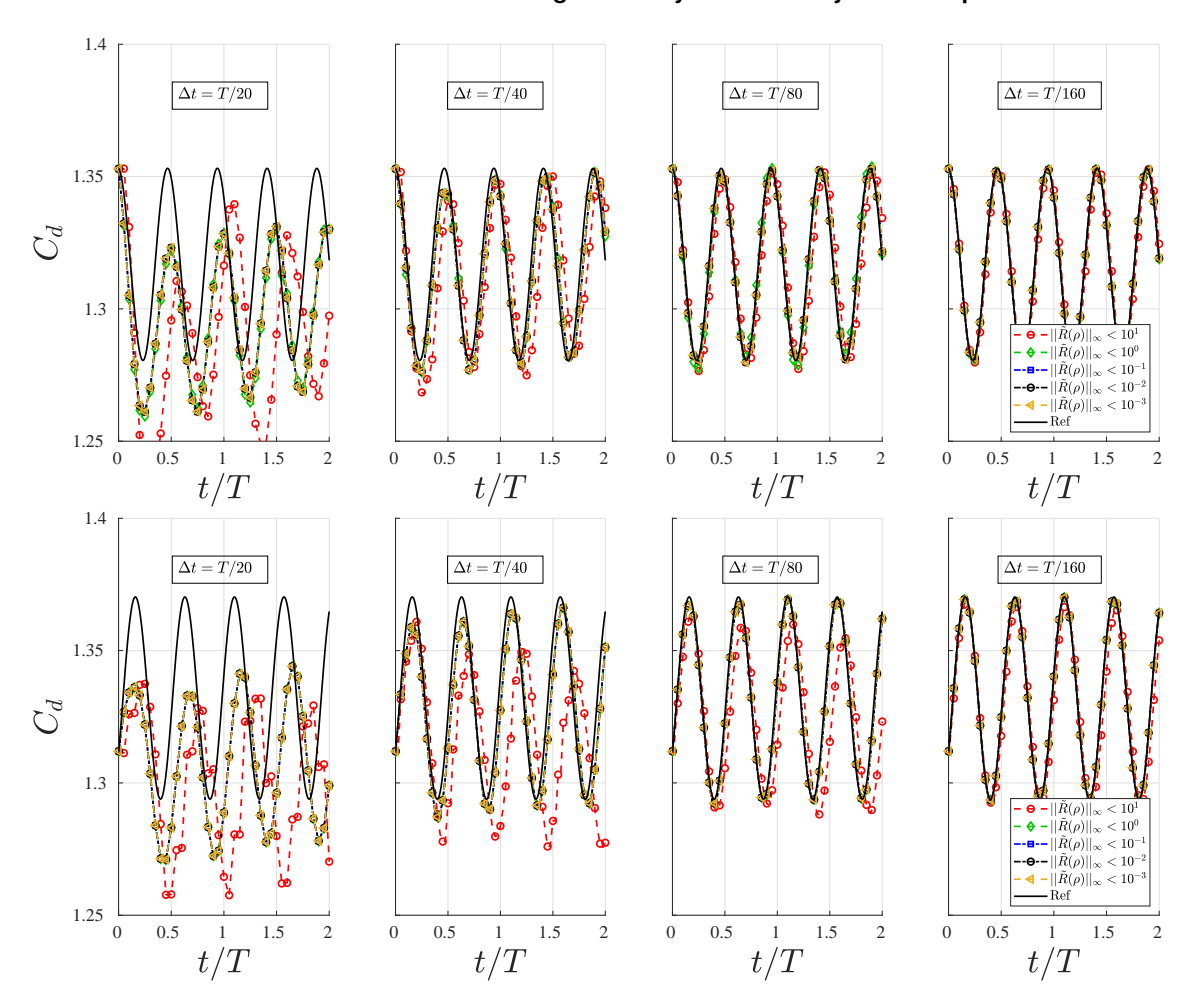


Figure 4 – Time evolution of drag over 1.5T of integrated drag with different convergence criterion. Comparisons to "excact" solution. From left to right: n = 20, 40, 80, 160. Results shown for coarsest grid (top), medium grid (bottom).

of inner iterations in dual time per non-linear solution are is displayed in Figure 5. We see that the errors converge as the number of non-linear iterations increase, most errors convergence within 3-4 inner iterations, depending on time step and grid refinement. It is noted that results were not acquired for time steps  $\Delta t = T/20, T/40$  on the finest grid, this is due to the non-linear solver converged poorly and is believed to depend on the finer time step being required to resolve the physics on the local grid resolution.

## 6.2 Unsteady Euler flow of RAE 2822 Airfoil

The second test case is the two-dimensional euler flow over the RAE 2822 airfoil, [15]. The derivatives  $C_{L,\alpha}, C_{L,\alpha}$  are computed for  $\alpha_0 = 3.0^\circ$ , for free stream Mach numbers  $M_\infty = 0.5$ ,  $M_\infty = 0.75$  and  $M_\infty = 1.2$ . Three successively refined unstructured grids consiting of triangle cells with  $16 \times 10^3$  (G1),  $63 \times 10^3$  (G2) and  $252 \times 10^3$  (G3) nodes are employed. Figure 6 shows a detail of the grid and the Mach number contours of the converged solution for the steady simulations.

The unsteady simulations are computed in a rotating coordinate frame of reference by employing Equations (28) and (36). The pitching amplitude is set to  $\alpha_{amp} = 0.1^{\circ}$  and the pitching frequencies f = [1, 1/2, 1/4, 1/8, 1/16, 1/32] Hz are considered. The pitching period T = 1/f is resolved with a time step  $\Delta t = T/100$  for all cases.

The convergence of the density residual for a typical global time steps and the lift coefficient as function of computational time are depicted in Figure 7. The convergence criterion for the simulations is set to 9 orders of residual reduction for the inner iterations. The simulation using the exact linearization of the Jacobian converges in around 7-8 inner iterations for  $M_{\infty} = 0.5$ , 14-15 inner iterations for  $M_{\infty} = 0.75$  and 12-13 inner iterations for  $M_{\infty} = 1.2$ . The convergence for the approximative Jacobian

### **Enhancing Efficiency For Unsteady CFD Computations in Aeronautics**

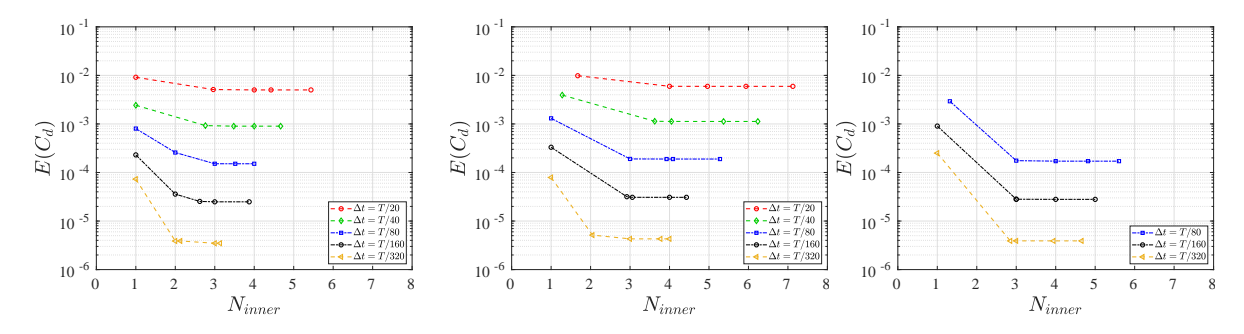


Figure 5 – L2-error of integrated drag over 1.5 periods with varying time steps. Error as a function of number of mean interations,  $N_{inner}$ , per non-linear solution. Results for coarsest grid (left), medium grid (middle), finest grid (right).

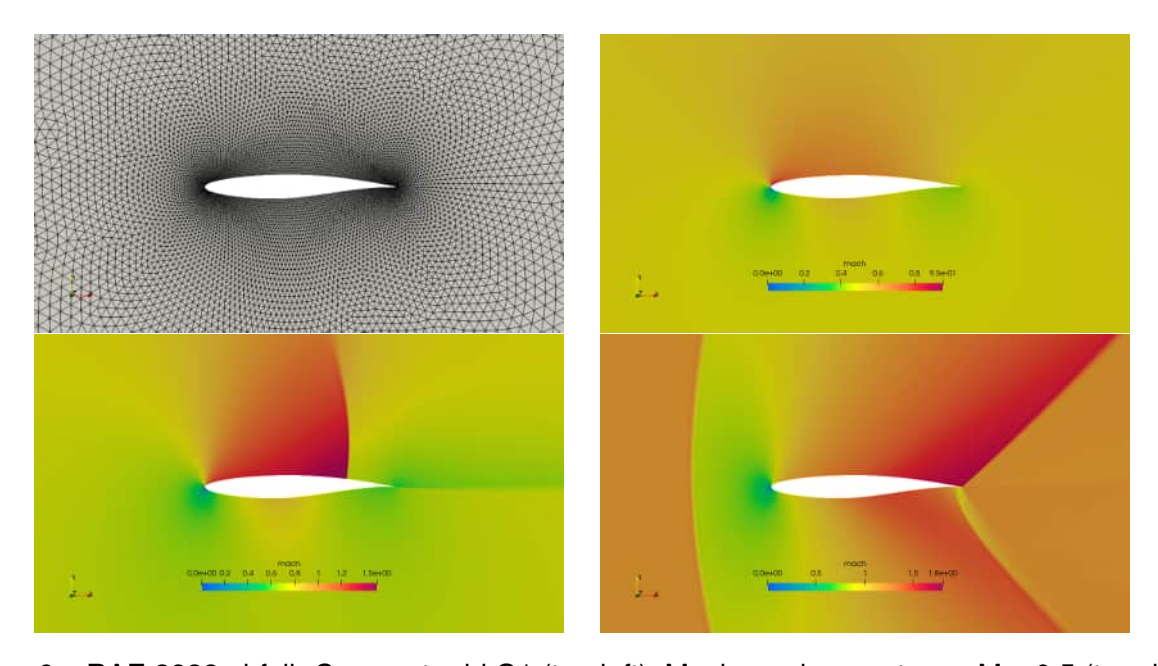


Figure 6 – RAE 2822 airfoil. Coarsest grid G1 (top left), Mach number contours, M = 0.5 (top right), M=0.75 (bottom left), M=1.2 (bottom right).

is far worse and requires more than 400 inner iterations for all Mach numbers considered. The response in  $C_L$  shows a sinusoidal behaviour for all three Mach numbers, veryfing that the ansatz given by Equation (34) is valid.

The estimated coefficients are presented in Figures 8 and 9. It can be seen that as the pitching frequency is decreased, the estimated values of  $C_{L,\alpha}$  and  $C_{L,\dot{\alpha}}$  are tending to a constant value. As expected, the estimated value of the  $C_{L,\alpha}$  coefficient is almost two orders larger than the  $C_{L,\dot{\alpha}}$  coefficient. It is also verified that the terms containing higher frequencies (n > 1 in Equation (37)) are 3-4 orders smaller than the  $C_{L,\dot{\alpha}}$  coefficient.

The computed dynamic coefficients for the three Mach numbers on the finest grid G3 are displayed in Table 1. The values for the lowest frequencey (f=0.03125) are displayed together with values at  $\omega=0$  (f=0) obtained by Richardson extrapolation. We conclude that the extrapolated values give an accurate estimate and are close to the values obtained at the lowest frequency.

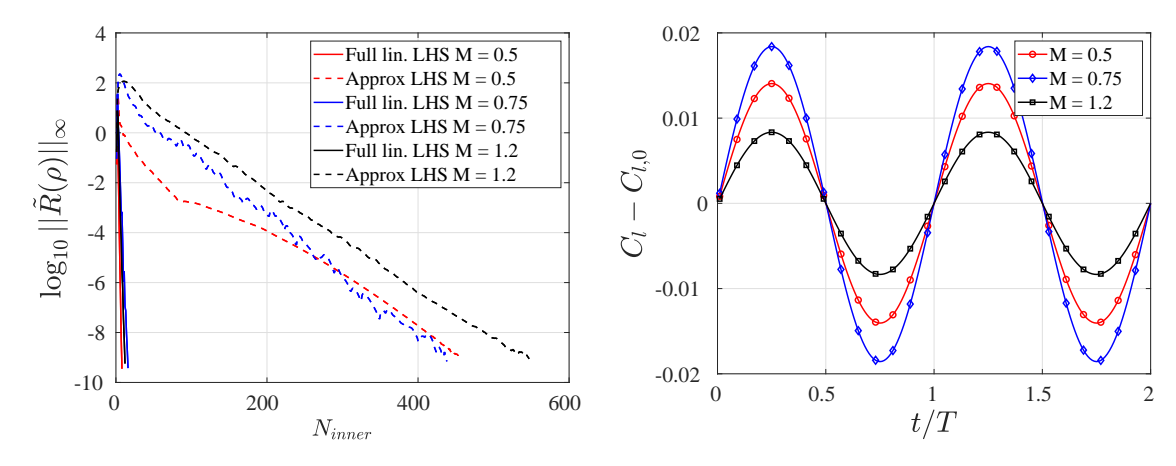


Figure 7 – RAE2822 convergence of density residual as function of inner iterations, one typical global time step shown (left). Evolution of lift coefficient as function of elapsed time (right). Results acquired on finest grid (G3) for f = 1/32 Hz.

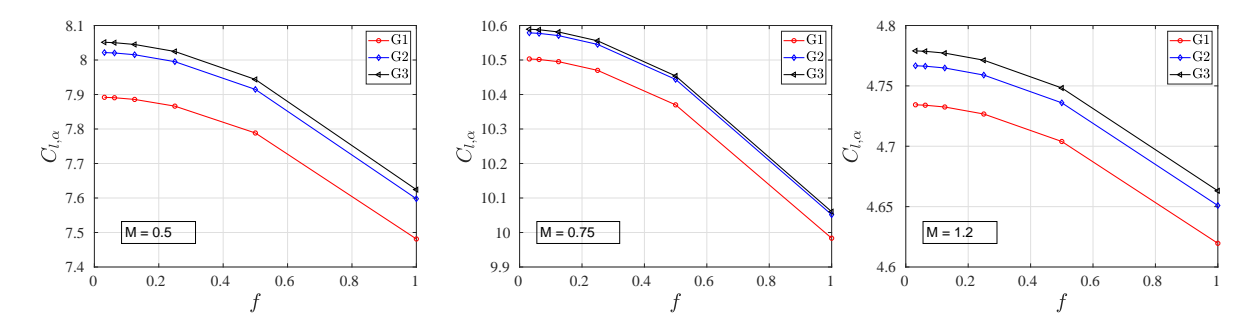


Figure 8 – Convergence of estimated  $C_{L,\alpha}$  coefficient as a function frequency (Hz) and grid resolution. Results shown for M = 0.5 (left), M = 0.75 (middle) and M = 1.2 (right).

## 7. Summary and Conclusions

We present work on an implicit discretization of the governing Navier-Stokes equations. The implicit approach is here employed for time dependent problems where we solve a state problem in dual time for each physical time step.

The implicit approach relies on the discretization of the non-linear governing equations using an Euler backward method. The residual is linearized leading to a linear sparse system of equations that are inverted iteratively with an ILU preconditioned GMRES method. We show that when all terms of the non-linear residual are linearized and combined with a large time step we can get extremely fast steady state convergence approaching quadratic convergence of a Newton method. Approximations in the linearization or under-relaxation of updates often lead to a drastic deterioration of the convergence and lower efficiency as we also demonstrate.

Unsteady calculations are presented for a piching airfoil and vortex shedding behind a cylinder. We compute the dynamic derivate of lift for the piching airfoil and give some theory on how dynamic derivates are computed in general. We also show how these derivatives can be computed based on a steady state solution only which will be explored in the future. The derivates are computed with varying pitching frequencies and extrapolated to zero frequency based on Richardson extrapolation.

$M_{\infty}$	$C_{L,\dot{\alpha}}(f=0.03125)$	$C_{L,\dot{\alpha}}(f=0)$
0.5	-0.102660	-0.102675
0.75	-0.189283	-0.189305
1.2	-0.013457	-0.013463

Table 1 – Dynamic derivatives of the lift coefficient at  $M_{\infty}=0.5,0.75,1.2$  on the finest grid. Values for the lowest frequencey ( $C_{L,\dot{\alpha}}(f=0.03125)$ ) and Richardson extrapolated values  $C_{L,\dot{\alpha}}(f=0)$ 

## **Enhancing Efficiency For Unsteady CFD Computations in Aeronautics**

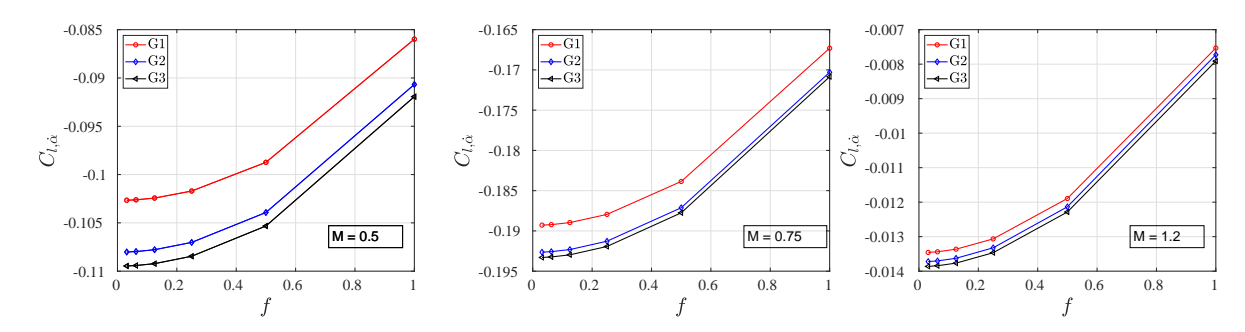


Figure 9 – Convergence of estimated  $C_{L,\dot{\alpha}}$  coefficient as a function frequency (Hz) and grid resolution. Results shown for M = 0.5 (left), M = 0.75 (middle) and M = 1.2 (right).

The pitching is done at a subsonic, transonic and supersonic Mach number for which excellent convergence rates are obtained in dual time regardless the Mach number. The vortex shedding over a cylinder is carried out for a low Mach number and various grid sizes. As for the pitching airfoil superior convergence is obtained with a proper linearization of all terms of the non-linear residual. An investigation of required number of iterations in dual time reveals that only about three iterations in dual time per time step is required to reach a time dependent solution, provided the time step is sufficiently fine to resolve the unsteadiness.

## 8. Contact Author Email Address

Mailto: peter.eliasson2@saabgroup.com

# 9. Copyright Statement

The authors confirm that they, and/or their company or organization, hold copyright on all of the original material included in this paper. The authors also confirm that they have obtained permission, from the copyright holder of any third party material included in this paper, to publish it as part of their paper. The authors confirm that they give permission, or have obtained permission from the copyright holder of this paper, for the publication and distribution of this paper as part of the ICAS proceedings or as individual off-prints from the proceedings.

## References

- [1] Hackström, M., Kållberg, F., Nordström, P. Aerodynamic development of Saab FCAS unmanned supersonic combat aircraft *International Council of the Aeronautical Sciences, ICAS*, ICAS paper 2022\_0570, Stockholm, 2022.
- [2] Eliasson, P., Eriksson, S. and Nordström, J. The influence of weak and strong solid wall boundary conditions on the convergence to steady-state of the Navier-Stokes equations. *AIAA Paper*, No. 2009-3551, 2009.
- [3] Eliasson, P., Weinerfelt, P. and Nordström, J. Application of a line-implicit scheme on stretched unstructured grids. *AIAA Paper*, No. 2009-016, 2009.
- [4] Eliasson, P., Weinerfelt, P., Bramkamp, F. Enhancing CFD predictions for the Gripen aircraft, *International Council of the Aeronautical Sciences, ICAS*, ICAS paper 2022\_0242, Stockholm, 2022.
- [5] Eliasson P. EDGE, a Navier-Stokes solver for unstructured grids. FOI report, FOI-R-0298-SE, Swedish Defence Research Agency (FOI). Stockholm (Sweden), 2001.
- [6] Langer, S. Investigation and application of point implicit Runge-Kutta methods to inviscid flow problems. Int. J. Numer. Meth. Fluids, 69: 332-352, 2012.
- [7] Langer, S. Agglomeration multigrid methods with implicit Runge-Lutta smoothers applied to aerodynamic simulations on unstructured grids, Journal of Computational Physics, 277: 72-100, 2014.
- [8] Saad, Y. and Schultz, M. H. GMRES: A generalized minimal residual algorithm for solving nonsymmetric linear systems, *SIAM Journal of Scientific and Statistical Computing*, Vol. 7, No. 3, pp. 856-869, 1986.
- [9] Balay, S., Gropp, W. D., McInnes, L. C. and Smith, B. F. Efficient management of parallelism in object oriented numerical software libraries, *Modern Software Tools in Scientific Computing*, Birkhäuser Press, pp. 163-202, 1997.
- [10] Jameson, A. Time dependent calculations using multigrid, with applications to unsteady flow past airfoils and wings. *AIAA Paper*, 91-1596, 1991.

### **Enhancing Efficiency For Unsteady CFD Computations in Aeronautics**

- [11] Eliasson, P. and Weinerfelt, P. High-order implicit time integration for unsteady turbulent flow simulations, *Computer & Fluids*, Vol. 112, pp. 35-49, 2015.
- [12] Jameson, A. Evaluation of fully implicit Runge-Kutta schemes for unsteady flow calculations, *Journal of Scientific Computing*, DOI 10.1007/s10915-017-0476-x, 2017.
- [13] Eliasson, P. and Weinerfelt, P. Recent applications of the flow solver Edge, Proc. to 7th Asian CFD Conference, Bangalore, India, 2007.
- [14] Nordström, J., Eriksson, S. and Eliasson, P. Weak and strong wall boundary procedures and convergence to steady state of the Navier-Stokes equations, *Journal of Computational Physics*, Vol. 231, pp. 4867-4884, 2012.
- [15] Cook, P., Donald, M., Formin, M. Aerofoil Rae 2822 Pressure distributions and boundary layer and wake measurements, *AGARD Report AR*, Vol. 138, pp. A6.1-A6.77, 1979.